Xingli Zhao
State Key Laboratory of Reliability and Intelligence of Electrical Equipment, Hebei University of Technology, 8, No. 1 Dingzigu Road, Hongqiao District, Tianjin 300131, China;
Hebei Key Laboratory of Robot Sensing and Human-Robot Interaction, Hebei University of Technology, 8, No. 1 Dingzigu Road, Hongqiao District, Tianjin 300131, China;
School of Mechanical Engineering, Hebei University of Technology, 8, No. 1 Dingzigu Road, Hongqiao District, Tianjin 300131, China
e-mail: 201811201023@stu.hebut.edu.cn

Shijie Guo[1]
State Key Laboratory of Reliability and Intelligence of Electrical Equipment, Hebei University of Technology, 8, No. 1 Dingzigu Road, Hongqiao District, Tianjin 300131, China;
Hebei Key Laboratory of Robot Sensing and Human-Robot Interaction, Hebei University of Technology, 8, No. 1 Dingzigu Road, Hongqiao District, Tianjin 300131, China;
School of Mechanical Engineering, Hebei University of Technology, 8, No. 1 Dingzigu Road, Hongqiao District, Tianjin 300131, China
e-mail: guoshijie@hebut.edu.cn

Sen Xiao
School of Mechanical Engineering, Hebei University of Technology, 8, No. 1 Dingzigu Road, Hongqiao District, Tianjin 300131, China
e-mail: xiaosen@hebut.edu.cn

Yao Song
State Key Laboratory of Reliability and Intelligence of Electrical Equipment, Hebei University of Technology, 8, No. 1 Dingzigu Road, Hongqiao District, Tianjin 300131, China;
Hebei Key Laboratory of Robot Sensing and Human-Robot Interaction, Hebei University of Technology, 8, No. 1 Dingzigu Road, Hongqiao District, Tianjin 300131, China
e-mail: april_songyao@163.com

Thorax Dynamic Modeling and Biomechanical Analysis of Chest Breathing in Supine Lying Position

During respiration, the expansion and contraction of the chest and abdomen are coupled with each other, presenting a complex torso movement pattern. A finite element (FE) model of chest breathing based on the HUMOS2 human body model was developed. One-dimensional muscle units with active contraction functions were incorporated into the model based on Hill's active muscle model so as to generate muscle contraction forces that can change over time. The model was validated by comparing it to the surface displacement of the chest and abdomen during respiration. Then, the mechanism of the coupled motion of the chest and abdomen was analyzed. The analyses revealed that since the abdominal wall muscles are connected to the lower edge of the rib cage through tendons, the movement of the rib cage may cause the abdominal wall muscles to be stretched in both horizontal and vertical in a supine position. The anteroposterior and the right–left diameters of the chest will increase at inspiration, while the right–left diameter of the abdomen will decrease even though the anteroposterior diameter of the abdomen increases. The external intercostal muscles at different regions had different effects on the motion of the ribs during respiration. In particular, the external intercostal muscles at the lateral region had a larger effect on pump handle movement than bucket handle movement, and the external intercostal muscles at the dorsal region had a greater influence on bucket handle movement than pump handle movement.
[DOI: 10.1115/1.4054346]

Keywords: respiratory biomechanics, surface displacement, active muscle model, rib cage motion

[1]Corresponding author.
Manuscript received September 1, 2021; final manuscript received April 6, 2022; published online May 6, 2022. Assoc. Editor: Matthew B. Panzer.

1 Introduction

Respiratory motion prediction plays an important role in the diagnosis and treatment of respiratory diseases and tumor radiotherapy. For example, the medical standard for the diagnosis of sleep apnea syndrome requires the monitoring of the expansion and contraction of the chest and abdomen [1], the diagnosis of chronic obstructive pulmonary disease requires the measurement of airflow and lung deformation during respiration [2], and the accurate identification of tumor locations during radiation therapy requires considerations of respiratory motion compensation [3].

To improve the accuracy of the diagnosis and treatment of respiratory diseases, and the efficacy of tumor radiotherapy, many researchers have studied the respiratory motion of the chest and abdomen. Currently, studies of respiratory motion mainly include two methods: image-based and model methods. The first methods estimate the relationships between the movement of chest organs and surface deformation using medical images and aim to track organ movement during radiotherapy or other respiratory disease treatments, such as magnetic resonance imaging or computerized tomography scans [4,5].

The first methods are accurate and reliable, but they cause harm to the human body and are expensive. For example, computerized tomography is accurate in tracking the motions of internal organs during respiration. However, it is harmful to both patients and doctors due to the use of radioactive rays. Meanwhile, magnetic resonance imaging requires the patient to be in a confined space for a long time, causing fear and ear discomfort [6]. Based on such challenges, mechanical models have been proposed to study respiratory motion. Some researchers established simplified mechanical models by abstractly treating the chest and abdomen as spring-mass models or compartment models to characterize the respiratory movement [7–9]. The advantages of simplified mechanical models are that they are easy to solve and they help explain the mechanisms of respiratory motion. However, the human body is a highly nonlinear continuum, so the accuracy of simplified mechanical models is not typically high. The finite element (FE) method has many advantages for solving nonlinear problems that can improve model accuracy. The FE models refer to virtual experiments and have been used to solve medical and engineering problems, such as pathological analysis [10,11], virtual surgery [12], and studies of occupant injury for collision protection [13]. The FE models can be used to obtain the stress, strain, and interaction forces between tissues, which is necessary to reveal the mechanisms of respiratory motion.

To establish highly accurate FE models, many researchers have performed numerous different studies. For respiratory motion modeling of the lung, several biomechanical models based on thoracic image data and the FE model have been proposed to accurately estimate respiratory tumor motion or deformation [14,15]. To study the biomechanics of the rib cage, Didier et al. [16] studied the human rib displacements using the finite helical axis method. Loring et al. [17] established a rib cage model with several beam elements and analyzed rib kinematics under the action of respiratory muscles in the 1990s. However, due to the limitations of computer technologies at that time, the accuracy of that model was not high. Zhang et al. [18] established an FE model of the thorax to characterize the motion of the ribs under the action of the intercostal muscles at different regions. However, the costovertebral joints in the model were based on the spherical joints, which did not take into account the differences in stiffness between different joint axes. Behr et al. [19] established a three-dimensional model of respiration based on the HUMOS2 model and the angular rotation of the ribcage in the sagittal plane were considered to evaluate the response of the model. However, the respiratory motion of the chest and abdomen was not analyzed. Thus, the coupled motion of the chest and abdomen during respiration requires further analysis.

Lying in supine position is required for the diagnosis and treatment of most respiratory diseases and tumor radiotherapy in clinics. As more than 50% of adults use chest breathing at rest, chest breathing while in supine position was evaluated in this study. The study was carried out in the following aspects: First, a chest breathing finite element model with active intercostal muscles was developed for respiratory mechanics investigation. Its parameters were optimized by comparing with experiments. Second, the relationship between the muscle force of chest breathing and the coupled thoracoabdominal motion was analyzed, and the mechanism of the coupled motion of the chest and abdomen was investigated. Finally, rib kinematics caused by the intercostal muscles at different regions were discussed.

2 Materials and Methods

2.1 Development of the Human-Mattress Model in Supine Position. The human-mattress model included a mattress, the ground, and the chest and abdomen of the pedestrian HUMOS2 model (Fig. 1(*a*)). The HUMOS2 model was developed by the European Union Human Security Research Program to study human bodily injury caused by automobile collisions, and its validity has been verified [20–22]. The model includes soft tissues (skin, flesh, and muscles), bones, and organs, with the data for each coming from the anatomy of a human trunk, which is then independently divided by finite element meshing (Fig. 1(*b*)). The skin and flesh are connected by shared nodes, the bones are connected by one-dimensional spring elements or two-dimensional shell elements that simulate the connection of ligaments, and the contact conditions were applied between adjacent organs and bones to prevent the intersection of regions. The mattress is made of a foam based on the viscoelastic material model, and an infinite rigid wall was used to simulate the ground. The contact mode between the human model and the mattress was based on the penalty method. The human and the mattress were set to slide with friction. The friction coefficient between human body and the mattress was set to 0.3 [23]. The gravity field was

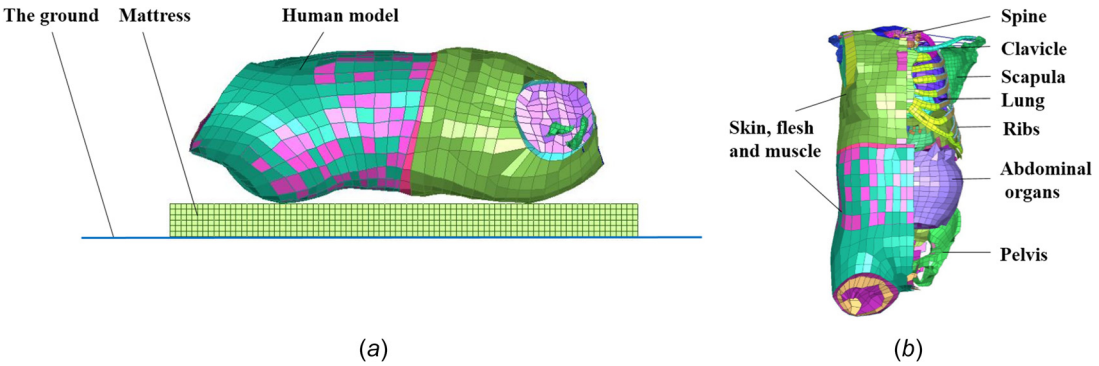

Fig. 1 The dynamic model of chest breathing (*a*), and the profile of the chest and abdomen of the HUMOS2 model (*b*)

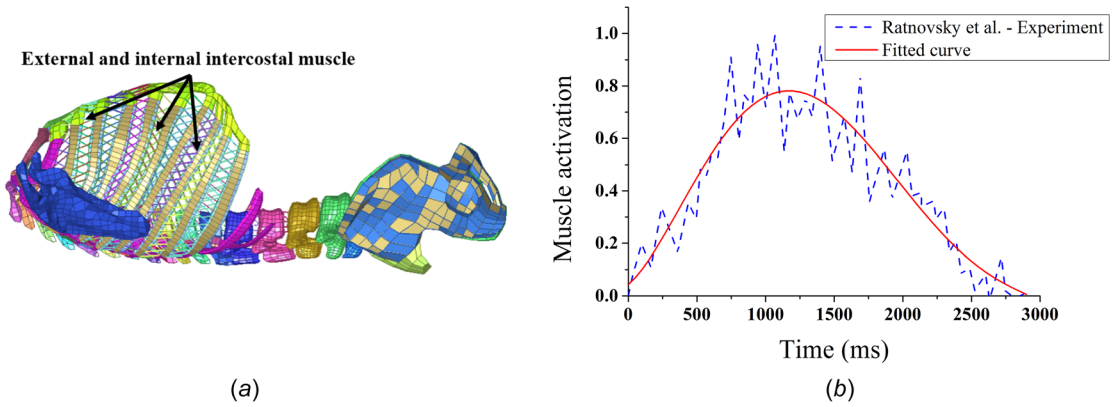

Fig. 2 Developed active intercostal muscles (*a*) based on Hill's active muscle model and the fitted muscle activation curve (*b*)

applied in the complete model, and its direction was vertically downward.

2.2 Development of Active Respiratory Muscles and Joints. Breathing patterns are mainly divided into chest breathing, abdominal breathing, and a mixture of both types of breathing. Chest breathing is characterized by significant chest expansion and contraction, while abdominal breathing, also called deep breathing, is characterized by significant abdominal expansion and contraction. The power sources of respiratory movement are the respiratory muscles, which mainly include intercostal muscles, the diaphragm, abdominal wall muscles, the sternocleidomastoid muscle, and the trapezius muscle. Chest breathing is mainly attributed to the intercostal muscles and accessory muscles, and the role of intercostal muscles was analyzed in this study [24–26]. However, existing commercial human models, including the HUMOS2 model, are unable to simulate respiratory movement directly because the respiratory muscles in such models are passive continuums. For this reason, active intercostal muscles using Hill's active muscle model were incorporated into the HUMOS2 model. Hill's active muscle model is the most widely used skeletal muscle model, and includes three elements: the contractile unit, the series elastic unit, and the parallel elastic unit, which can simulate the active and passive responses of muscles [27].

The intercostal muscles, with an outer layer, and the external intercostal muscles, with an inner layer, the internal intercostal muscles, are located in the interspaces between adjacent ribs [28]. The fibers of the external intercostal muscles run obliquely and anteroinferiorly from the lower edge of the upper ribs to the upper edge of the lower ribs, while the fibers of the internal intercostal muscles run obliquely and posteroinferiorly from the lower edge of the upper ribs to the upper edge of the lower ribs [29,30]. In this study, we established the external and internal intercostal muscles from the first rib to the tenth rib. The eleventh and twelfth ribs are floating, and were not considered.

Based on Hill's muscle model, the active intercostal muscles were modeled by a series of spring elements, which described a user-defined viscoelastic material in a commercial explicit code (RADIOSS). The number of the internal intercostal muscle elements was 330. Among them, the ventral portion of the internal intercostal muscle (parasternal intercostal muscle) elements was 52 and the lateral portion of the internal intercostal muscle elements was 278. The number of the external intercostal muscle elements was 446. Among them, the lateral portion of the external intercostal muscle elements was 292 and the dorsal portion of the external intercostal muscle elements was 154. Figure 2(*a*) shows the developed model of active external and internal intercostal muscles.

The Hill's muscle model used in this study is composed of a contractile unit in series of a series elastic unit, which are both in parallel with a parallel elastic unit [27,31]. The response of the muscle was determined by the following formulae:

$$\begin{cases} F_{\text{Mus}} = F_{\text{CE}} + F_{\text{PE}} \\ F_{\text{CE}} = F_{\text{SE}} \end{cases} \tag{1}$$

where F_{Mus} is the total muscle force, and F_{CE}, F_{PE}, and F_{SE} are the forces developed by the contractile, parallel, and series units, respectively. The active force of the muscle can also be approximately estimated by

$$\begin{cases} F_{\text{CE}} = F_{\max} \cdot A(t) \cdot f_{\text{a}}(\lambda) \cdot \alpha \\ F_{\max} = PCSA \cdot \sigma_{\max} \end{cases} \tag{2}$$

where $F_{\max}$ is the maximum isometric force under optimal length, which can be obtained by the product of the equivalent physiological cross-sectional area (PCSA) of the target muscle and the maximum stress $\sigma_{\max}$ of the muscle fiber [32,33]. The thickness of the external intercostal muscle increased gradually from lateral to dorsal. This change in thickness was expressed by reducing the spacing between adjacent active muscle springs while PCSA was set as 70 mm^2 according to the distance between muscle springs and the thickness of the actual intercostal muscle [34]. The peak muscle stress value, $\sigma_{\max}$, was set to 1 MPa [35]. $A(t)$ is the curve of the relationship between time and the muscle activation level. The activation curve of the intercostal muscles was obtained by fitting the measured data in reference [36] by using a fifth-order polynomial (Fig. 2(*b*)).

This activation curve was used as a basic curve shape of muscle activation for different intercostal muscles in the simulation, but

Table 1 Properties of the active intercostal muscles added in the model

			The activation levels of the external intercostal muscles at lateral portion					
$F_{\max}$	PCSA	C_{sh}	First to third intercostal spaces			Fourth to sixth intercostal spaces		
70 N	70 mm^2	0.8	0.928	0.697	0.464	0.232	0.001	0.001

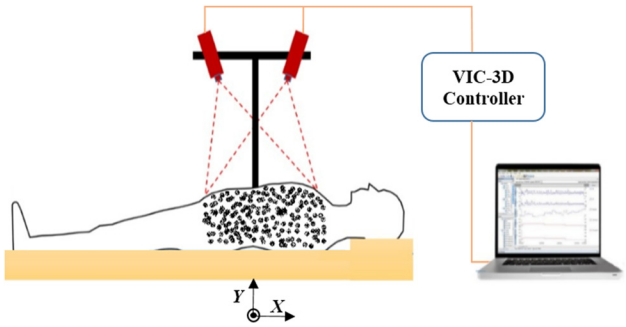

Fig. 3 The experimental setup

the activation time and magnitude were different. Inspiratory muscles were activated at the beginning of inspiration to reach their maximum activation toward the end of inspiration, while expiratory muscles were activated at the beginning of expiration to reach their maximum activation at midexpiration. This time shift was determined according to Ratnovsky et al. [26]. Besides, a scaling factor α was introduced to adjust the activation level of intercostal muscles at different intercostal spaces. The magnitude $A(t)$ was determined based on Wilson's research [37], where the activation level of the external intercostal muscles decreases when the number of ribs increases. The activation levels of the external intercostal muscles at the lateral portion are summarized in Table 1. $f_a(\lambda)$ is the active force-length relationship of the muscle [38,39]

$$f_a(\lambda) = 1.25\left\{\exp\left[-\left(\frac{\lambda-1}{C_{sh}}\right)^2\right]\right\} \tag{3}$$

where λ is the stretch ratio of the muscle and C_{sh} is a shape parameter which determines concavity of the muscle force-length characteristics [40].

The passive component of the muscle force is given by

$$F_{PE} = \begin{cases} \dfrac{F_{max}}{\exp(C_{PE})-1}\left[\exp\left(\dfrac{C_{PE}}{1.05}\cdot(\lambda-1)\right)-1\right], & \text{for} \quad \lambda > 1 \\ 0, & \text{otherwise} \end{cases} \tag{4}$$

where C_{PE} is the shape parameter of the muscle force-elongation characteristics of the parallel elastic element. Here, the C_{PE} was assumed to be 8 [40].

During breathing, the ribs rotate around the spine through the costovertebral joint, which is a composite joint with three rotational degrees-of-freedom. The stiffness of each axis of rotation is different and changes with changes in rotation angle. Thus, the stiffness and damping of the costovertebral joint in the HUMOS2 model were optimized according to relevant literature [41,42].

2.3 Simulation of the Dynamic Model of Chest Breathing. The simulation was divided into two stages: The first stage was a postural adjustment. Since the pedestrian model of HUMOS2 is a standing model, the positions of the internal organs and other soft tissues in human chest and abdomen differ with posture due to the existence of gravity. The internal organs and other soft tissues are close to the back in supine position as compared with a standing posture. Therefore, gravity load was applied to the human model to press the human body onto the mattress, and the soft tissues were deformed by gravity. Finally, the whole human body reached its position at the balance between gravity and mattress support. The second stage was to simulate the chest breathing movement in supine position; that is, to control the contraction and relaxation of the intercostal muscles and cause the expansion and contraction of the chest and abdomen. The two stages were conducted as two parts of a complete simulation, the simulation time for each stage was 2000 ms and 1000 ms, respectively. RADIOSS 2018 was used for the simulation, which was performed using an explicit solver. The average simulation time was 76 h with 3.5 GHz Intel Xeon processor core i7 and 64GB of RAM.

2.4 Validation of the Developed Model

2.4.1 Experiments of Surface Displacement. To verify the validity of the chest breathing model, an optical tracking system (VIC-3D system) was used to measure the chest and abdominal surface displacement of subjects during chest breathing in supine position (see Fig. 3). The VIC-3D system was developed by CSI Company in the United States. Two image acquisition devices were used to capture movements of the chest and abdomen during breathing. The three-dimensional surface displacement and strain of thoracoabdominal motion were measured with a measurement accuracy of 50 microstrains.

Twelve subjects were selected, aged 23–30 years, with a body mass index of 25.1 ± 7.7. All subjects were in good health and had no history of respiratory diseases. After reading the purpose and process of this study in detail, the subjects signed the informed consent form. The study abided by the ethical principles of the Declaration of Helsinki and the experiment was approved by the ethics committee of the North China University of Science and Technology Affiliated Hospital, Hebei, China. The subjects laid on a mattress while the experimenter applied a 75% speckle density to the surface of the subject's chest and abdomen at the beginning of each experiment. Each subject was instructed by the

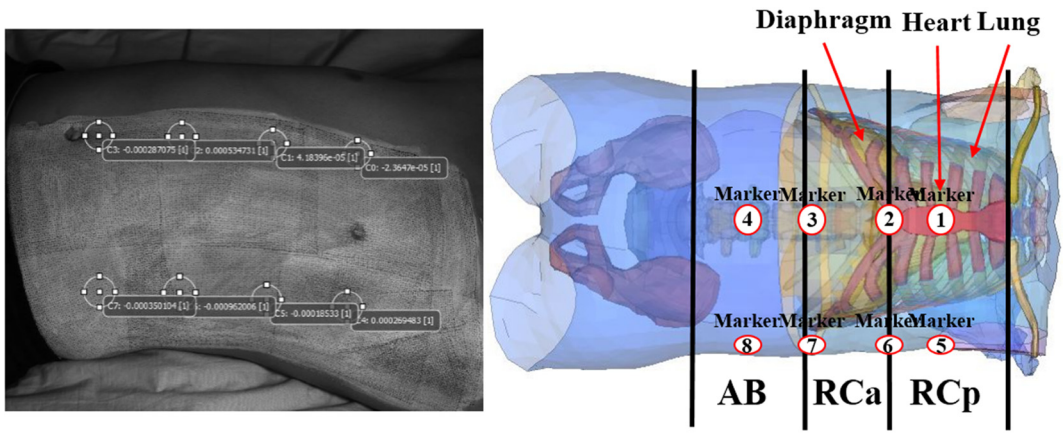

Fig. 4 The measurement areas of the surface displacement experiment

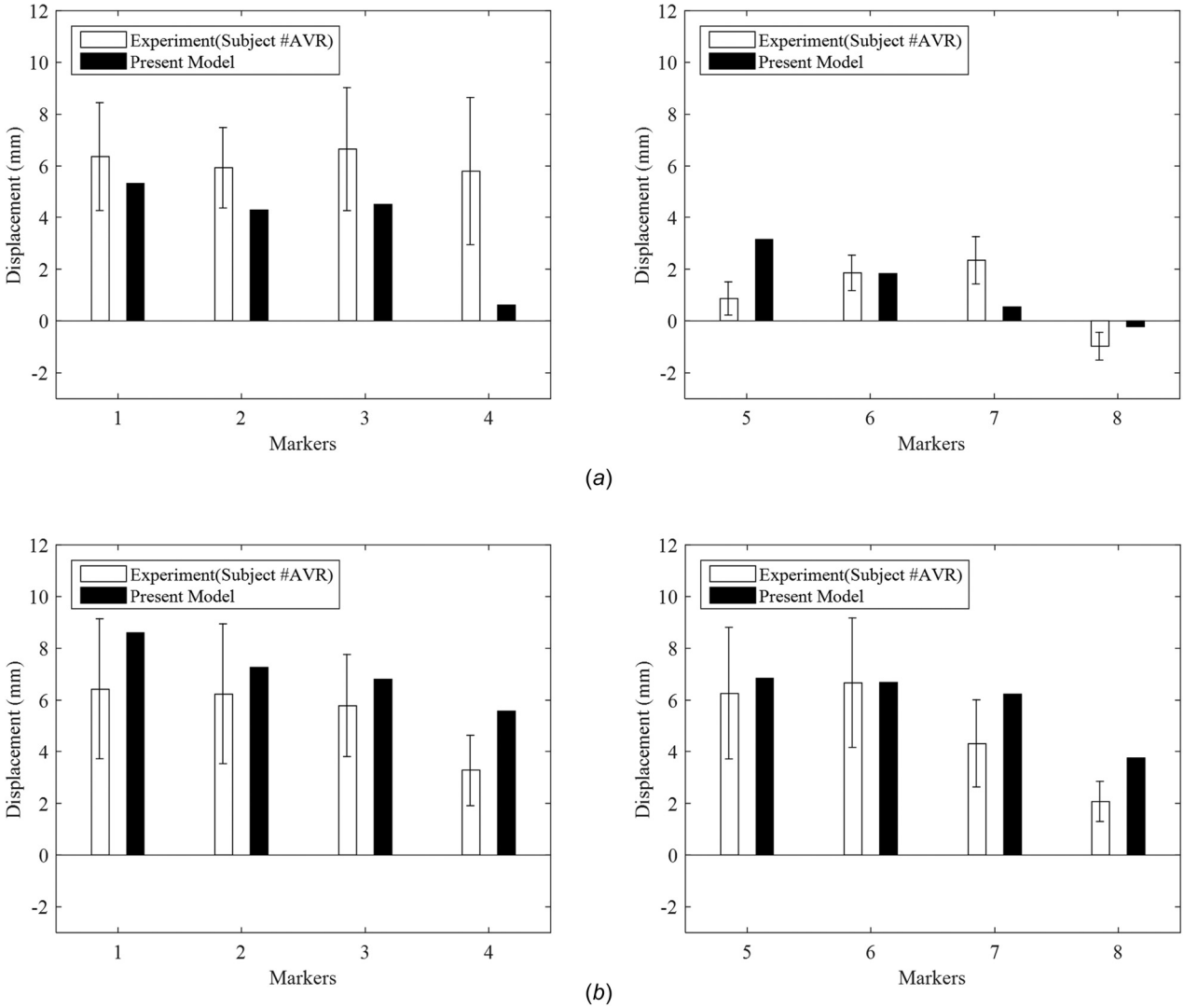

Fig. 5 Comparison of the normal surface displacement (*a*) and tangential surface displacement (*b*) at the chest and abdomen

experimenter to perform chest breathing (i.e., breathing using the upper chest) for 1 min, while the VIC-3D system collected surface displacement data for the chest and abdomen.

2.4.2 Location of the Markers on the Chest and Abdomen. To determine the location of markers on the chest and abdomen, a three-compartment thoracoabdominal model was used, including the pulmonary rib cage (RCp), the abdominal rib cage (RCa), and the abdomen [43]. Eight markers were then selected to measure the expansion and contraction displacement (normal and tangential displacement) of each area on the horizontal and vertical plane of the chest and abdomen during chest breathing. As shown in Fig. 4, the body of the sternum (marker 1) at the RCp, the xiphoid process (marker 2) between the RCp and RCa, the umbilical portion (marker 4) at the abdomen, and the middle position of the xiphoid process and umbilical portion (marker 3) at the RCa were selected from the horizontal plane of the human body. From the vertical plane (lateral plane) of the chest and abdomen, along the midaxillary line, the corresponding positions of markers 1–4 were marked as markers 5–8, respectively, to measure the normal and tangential displacement of the vertical plane.

3 Results and Discussion

3.1 Comparisons of the Surface Displacement of the Chest and Abdomen. As shown in Fig. 5, the experimental bar chart represents the mean value of the breathing amplitude of the averaged experimental data of the ten subjects. The other two subjects were excluded because they had obvious abdominal breathing characteristics during the experiment, i.e., the abdominal expansion and contraction were obvious. The error bar of the experimental bar chart represents the standard deviation of the breathing amplitude. We defined the normal displacement pointing in the anterior direction and lateral extremes of the chest and abdomen as positive (i.e., in the direction of thoracoabdominal expansion), and the tangential displacement toward the cranial direction as positive. The mean normal displacement of markers 1–7 was all positive; however, the mean normal displacement of marker 8 was negative, indicating that the anteroposterior and the right-left diameters of the chest increased at inspiration, while the right–left diameter of the abdomen decreased even though the anteroposterior diameter of the abdomen increased. The mean tangential displacement of markers 1–8 was all positive, indicating that the surface displacement of the chest and abdomen occurred toward the cranial direction during the inspiration of the chest breathing.

Table 2 shows the normal surface displacement of each marker on the chest and abdomen of ten subjects during chest breathing. Table 3 shows the tangential surface displacement of each marker on the chest and abdomen of ten subjects during chest breathing.

3.2 The Mechanism of the Coupled Motion of the Chest and Abdomen. For the normal surface displacements of the chest and abdomen, the displacement of markers 1–7 was all positive,

Table 2 Normal surface displacement of each marker (unit: mm)

	Normal displacement of the horizontal plane				Normal displacement of the vertical plane			
	Marker 1	Marker 2	Marker 3	Marker 4	Marker 5	Marker 6	Marker 7	Marker 8
S1	7.82 ± 3.27	6.31 ± 2.76	6.36 ± 2.47	6.01 ± 2.77	0.33 ± 0.25	1.83 ± 0.79	2.70 ± 1.09	−1.53 ± 0.67
S2	7.49 ± 0.57	6.51 ± 0.52	5.86 ± 1.12	4.09 ± 1.17	1.73 ± 0.21	1.84 ± 0.20	1.67 ± 0.22	−1.24 ± 0.35
S3	5.65 ± 1.54	6.02 ± 1.70	5.45 ± 1.31	3.71 ± 0.87	0.83 ± 0.22	2.53 ± 0.68	3.16 ± 0.84	−0.72 ± 0.22
S4	5.21 ± 0.75	5.73 ± 0.86	7.79 ± 1.90	7.08 ± 2.09	0.68 ± 0.25	0.80 ± 0.27	1.55 ± 0.59	−1.09 ± 0.22
S5	5.75 ± 0.63	5.74 ± 0.55	5.06 ± 0.37	3.55 ± 0.57	0.45 ± 0.12	1.32 ± 0.35	1.65 ± 0.40	−0.43 ± 0.11
S6	5.50 ± 0.67	6.18 ± 0.76	9.05 ± 1.76	8.04 ± 1.73	1.06 ± 0.43	1.25 ± 0.48	1.90 ± 0.88	−1.34 ± 0.42
S7	6.81 ± 0.95	5.59 ± 0.94	7.64 ± 1.11	6.26 ± 1.15	2.12 ± 0.13	2.05 ± 0.17	1.95 ± 0.20	−0.63 ± 0.26
S8	7.96 ± 1.90	6.48 ± 1.28	8.34 ± 2.93	9.14 ± 2.64	0.26 ± 0.21	2.29 ± 0.39	3.21 ± 0.48	−1.26 ± 0.58
S9	4.45 ± 1.75	4.81 ± 1.68	4.20 ± 1.19	3.11 ± 1.07	0.74 ± 0.14	2.10 ± 0.52	2.56 ± 0.72	−0.54 ± 0.20
S10	6.30 ± 2.70	5.54 ± 2.17	7.00 ± 3.08	7.38 ± 3.85	0.52 ± 0.31	1.82 ± 0.68	2.49 ± 0.92	−1.28 ± 0.41

Values are expressed as mean ± SD.

Table 3 Tangential surface displacement of each marker (unit: mm)

	Tangential displacement of the horizontal plane				Tangential displacement of the vertical plane			
	Marker 1	Marker 2	Marker 3	Marker 4	Marker 5	Marker 6	Marker 7	Marker 8
S1	7.11 ± 3.12	5.88 ± 2.61	5.33 ± 2.33	3.70 ± 1.67	7.72 ± 3.50	7.71 ± 3.32	5.18 ± 2.18	2.28 ± 1.05
S2	10.36 ± 0.88	9.44 ± 0.79	7.58 ± 0.70	4.95 ± 0.54	8.79 ± 0.72	8.74 ± 0.69	4.94 ± 0.39	3.09 ± 0.27
S3	4.32 ± 1.17	4.43 ± 1.21	5.22 ± 1.42	3.07 ± 0.97	4.98 ± 1.33	5.61 ± 1.51	3.77 ± 1.02	2.25 ± 0.62
S4	8.19 ± 1.14	9.68 ± 1.40	7.92 ± 1.12	3.50 ± 0.74	6.86 ± 1.18	7.80 ± 1.34	5.85 ± 1.02	1.90 ± 0.29
S5	2.43 ± 0.76	2.50 ± 0.79	2.91 ± 0.95	1.64 ± 0.46	2.65 ± 0.65	3.01 ± 0.78	2.03 ± 0.53	1.21 ± 0.31
S6	8.27 ± 1.00	10.14 ± 1.35	8.51 ± 1.20	3.28 ± 1.74	7.37 ± 0.84	8.61 ± 1.08	6.47 ± 0.87	2.31 ± 0.52
S7	7.46 ± 0.91	7.09 ± 0.80	5.77 ± 0.76	3.69 ± 0.61	6.58 ± 0.82	6.94 ± 0.76	3.61 ± 0.47	2.28 ± 0.36
S8	6.70 ± 1.46	5.50 ± 1.16	5.34 ± 1.02	2.55 ± 1.48	7.73 ± 1.58	8.14 ± 1.63	5.13 ± 1.04	1.90 ± 0.84
S9	3.41 ± 1.32	3.51 ± 1.31	4.15 ± 1.54	2.57 ± 0.94	3.90 ± 1.41	4.46 ± 1.33	2.89 ± 1.04	1.70 ± 0.58
S10	6.15 ± 2.51	5.23 ± 2.07	4.87 ± 1.93	3.27 ± 1.10	6.72 ± 2.69	6.69 ± 2.59	4.38 ± 1.75	1.80 ± 0.77

Values are expressed as mean ± SD.

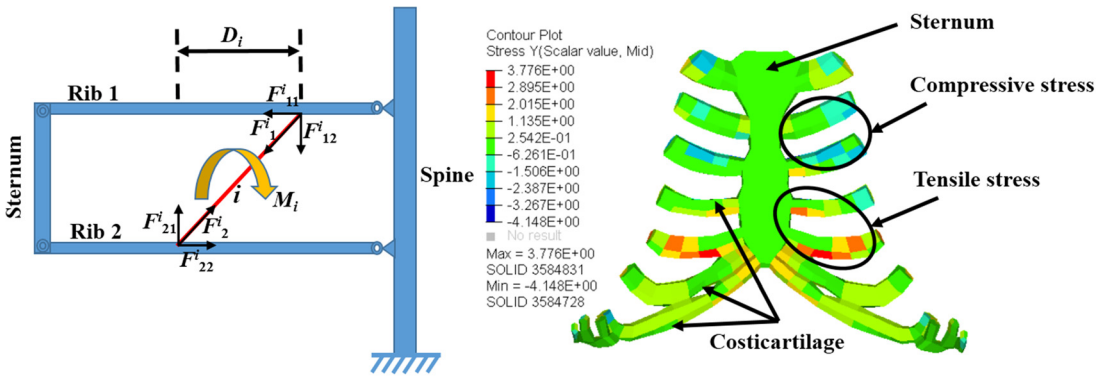

Fig. 6 Simplified mechanical model of inspiration (left) and the stress cloud diagram of costal cartilage (right)

while the displacement of marker 8 was negative. Thus, it was confirmed using the FE model that the abdominal muscles were subjected to tensile stress. When the subject was lying in supine position, the organs in the abdomen were affected by gravity such that the anteroposterior diameter of the abdomen decreased, while the right–left diameter increased. Because the abdominal wall muscles are attached to the lower margin of the rib cage by tendons, the movement of the ribs drives the abdominal wall muscles to passively stretch in the horizontal and vertical planes during inspiration. Thus, under such circumstances, the right–left diameter of the abdomen decreases, while the anteroposterior diameter increases. For the tangential surface displacement of the chest and abdomen, the displacement of markers 1–8 was all positive, which indicated that the soft tissues on the thoracoabdominal surface moved toward the cranial direction during inspiration of chest breathing.

A simplified mechanical model of chest breathing was developed to analyze the change in surface displacement caused by respiration, in which the ribs were assumed to be beam elements, with fixed hinge supports on the side of the spine and moving hinge supports on the side of the sternum. The contraction of the intercostal muscles during breathing causes the ribs to rotate around the costovertebral joints. This rotational moment is formed by the force of the intercostal muscles pulling the ribs (Fig. 6). For example, the muscle fiber i of the external intercostal muscle connects the lower edge of the upper Rib 1 (Fig. 6) and the upper edge of the lower Rib 2 (Fig. 6). A pair of forces, F^i_1 and F^i_2, are generated in the muscle fiber, i, when the intercostal muscles contract. This pair of forces can be decomposed into forces F^i_{12} and F^i_{21} that are perpendicular to the axis of the rib, and forces F^i_{11} and F^i_{22} that are along the axis of the rib. F^i_{12} and F^i_{21} are equal in magnitude and opposite in direction, and are separated by a distance

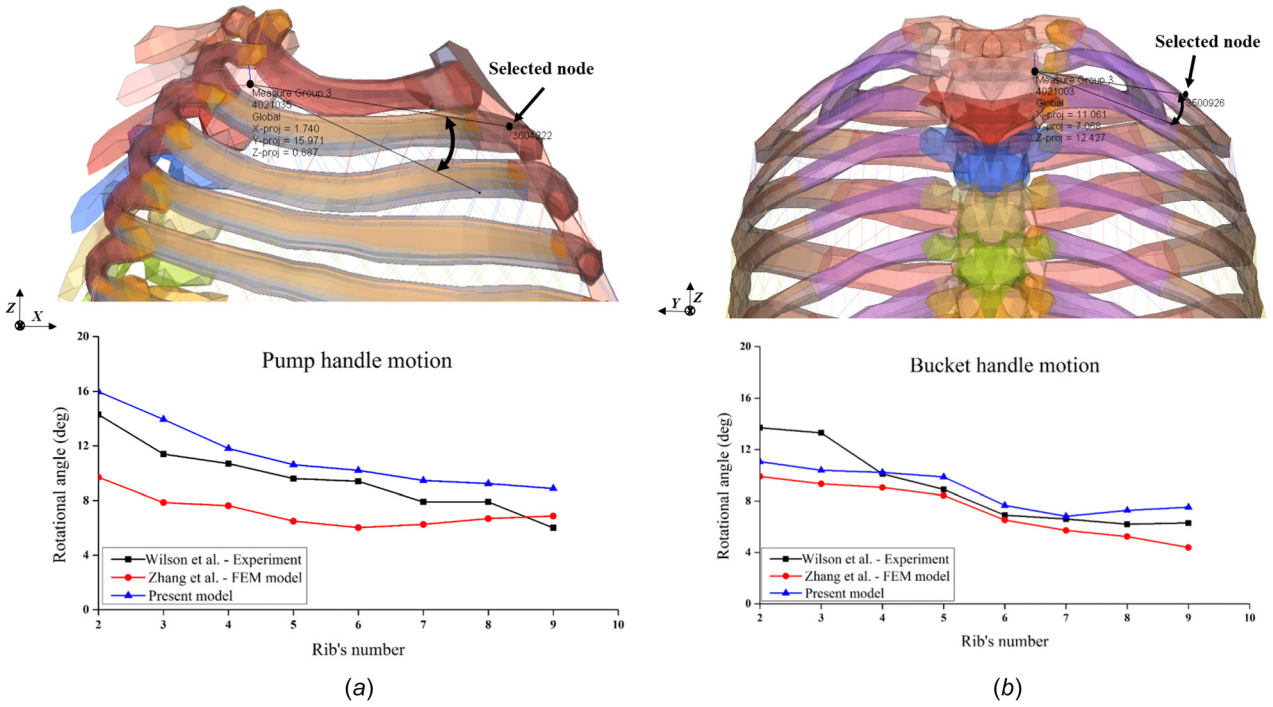

(*a*) (*b*)

Fig. 7 Comparisons of the pump handle angle (*a*) and bucket handle angle (*b*) of ribs to data from previous studies

D_i, forming a force couple, M_i. The total moment that acts on the rib is $M = \sum_i D_i \times F_{12}^i$, which causes the ribs elevated and rotated toward the cranial direction. F_{11}^i and F_{22}^i exert an axial tension and compression effect on the ribs, but due to the rib cage, the restriction of the costovertebral joint and the sternum, the axial displacement of the ribs is very small. The costal cartilage has a lesser rigidity and a greater elasticity than the sternum and ribs. The stress cloud diagram of costal cartilage shows that under the action of F_{11}^i and F_{22}^i, the upper costal cartilage is compressed and the lower costal cartilage is stretched.

3.3 The Kinematic Response of the Ribs

3.3.1 Development of the Musculoskeletal Model. The ribs play an important role in respiratory motion. To analyze the kinematics of the ribs at sagittal and coronal planes from functional residual capacity to total lung capacity, a musculoskeletal model was developed by removing the soft tissues from HUMOS2, while maintaining only the ribs, sternum, spine, and intercostal muscles. The boundary condition was that all the six degrees-of-freedom of the spinal nodes were clamped, as recommend by Loring [17]. Because the ribs rotated around the spine in supine position, the movement of the ribs would not be affected even if the six degrees-of-freedom of the spine were constrained. The external intercostal muscles and internal intercostal muscles were activated to achieve the maximum rotate angles of the ribs at sagittal and coronal planes in total lung capacity.

3.3.2 Validation of the Developed Musculoskeletal Model. The results were compared with those reported in previous experimental and computational studies [37,44]. To analyze the role of the intercostal muscles on the rib kinematics, the external intercostal muscles at different portions were activated, respectively. The alignment between the costovertebral joint of the corresponding rib and the costal cartilage tip was recorded, and the maximum projection angle during motion on the sagittal plane (*XZ* plane in Fig. 7(*a*)) was the pump handle angle. The alignment between the costovertebral joint of the corresponding rib and the margin of the dorsal rib was recorded, and the maximum projection angle in the motion process on the coronal plane (*YZ* plane in Fig. 7(*b*)) was the bucket handle angle.

3.3.3 Analysis of Rib Motion. The action of the ribs during chest breathing is the result of the associated action of the respiratory muscles. However, the role of the intercostal muscles in rib cage movement remains controversial. To explore this question, the role of the external and internal intercostal muscles during the movement of the ribs was evaluated. The external intercostal muscles were divided into the lateral portion and dorsal portion, as shown in Fig. 8.

The action of the ribs can be divided into the pump handle motion and the bucket handle motion during respiration. The former of which changes the dimensions of the thorax in the anteroposterior direction, while the latter of which changes the lateral dimensions of the thorax [30]. Here, three nodes, including the

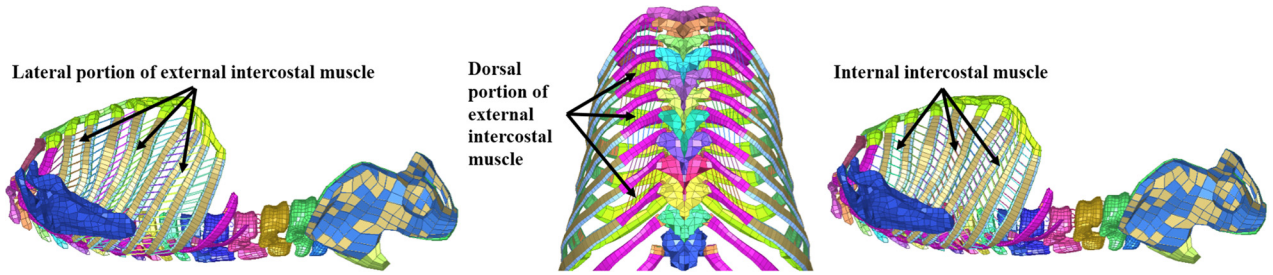

Fig. 8 Location of the external and internal intercostal muscles at different portions

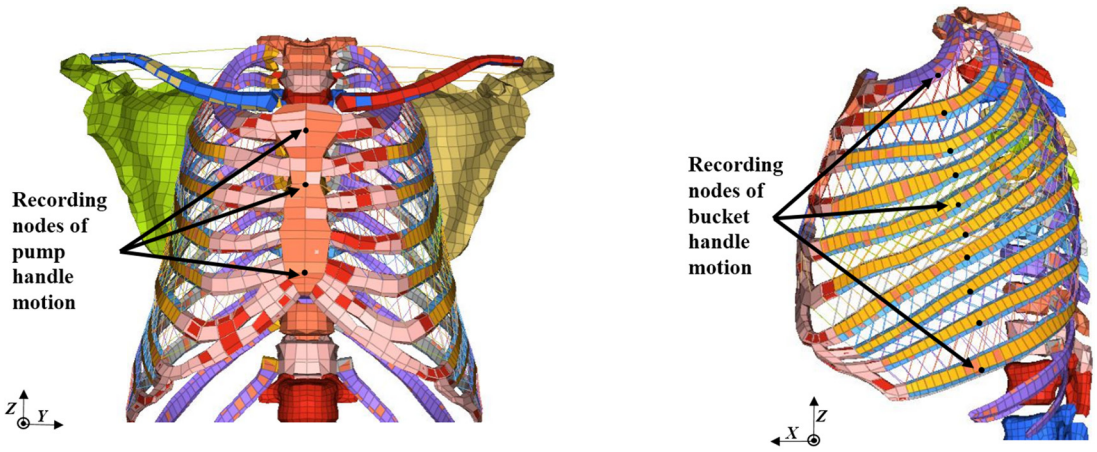

Fig. 9 Recording node of pump handle motion (*a*) and bucket handle motion (*b*)

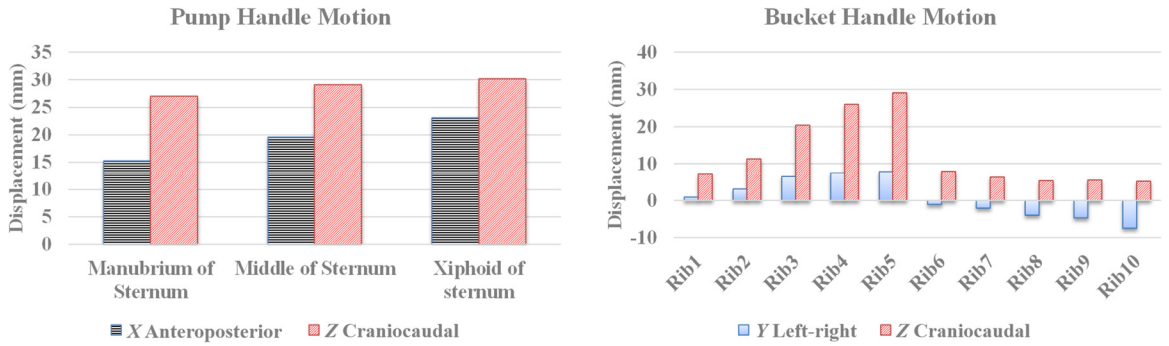

Fig. 10 Changes in pump handle motion and bucket handle motion of the ribs under the action of the lateral external intercostal muscles

manubrium of the sternum, the middle of the sternum, and the xiphoid process were selected to measure the pump handle motion, while the nodes on the outermost edge of ribs 1–10 ribs were selected to measure the bucket handle motion, as shown in Fig. 9.

Figure 10 shows the displacement of the ribs under the action of the lateral external intercostal muscles. The displacement of the manubrium of the sternum, the middle of the sternum, and the xiphoid process in the *X*-axis direction (anteroposterior direction) were 15.25, 19.58, and 23.09 mm, respectively. The displacements of nodes 1–10 in the *Y*-axis direction (lateral direction) were between −7.48 and 7.89 mm. The data illustrated that under the contraction of the lateral portion of the external intercostal muscles, the ribs exhibited pump handle (anteroposterior direction) and bucket handle motion (lateral direction), of which, pump handle motion was more significant than bucket handle motion. The displacements of bucket handle motion also increased from rib 1 to rib 5, while the displacements decreased from rib 5 to rib 10. Those data were due to the gradual decrease in muscle activation from rib 1 to rib 10, and a gradual increase in rib flexibility from rib 1 to rib 10 (action of costal cartilage). The kinematics of the rib under the action of the lateral external intercostal muscles was discussed in Sec. 3.2 on the mechanism of the coupled motion of the chest and abdomen (Fig. 6).

Figure 11 shows the numerical results of the pump handle motion and bucket handle motion caused by the contraction of the dorsal external intercostal muscles. The displacements in the *X*-axis direction (anteroposterior direction) were −26.27, −22.02, and −17.74 mm, respectively. The displacements in the *Y*-axis direction (lateral direction) were between −1.04 and 14.82 mm. The above results showed that the lateral portion of the ribs elevated and the sternum lowered, following the contraction of the dorsal external intercostal muscles.

The results were consistent with the experimental results of Sampson et al. [45], which found that subjects deformed their rib cage to a more elliptical shape (i.e., the anteroposterior diameter decreased and the right-left diameter increased) during loaded inspirations, which were associated with a marked increase in the inspiratory activity of the intercostal muscles situated near the midaxillary line, and a striking diminution of the activity near the parasternal area. The above results also illustrate that the ribs exhibited significant bucket handle motion when the dorsal intercostal muscles contracted and the displacements of the pump handle motion were negative.

It appears that the two fulcrums of the rib, the costovertebral joint and the sternocostal joint, caused the rib to turn up laterally under the action of the torque caused by the dorsal external intercostal muscles. When individuals lay in supine position, the spine can be regarded as being in a fixed state, and the displacement of the costovertebral joint is small. However, the cartilage is flexible and the sternocostal joint moves the sternum inferior and posterior under the action of the torque caused by the dorsal external intercostal muscles. Thus, under such conditions, the right–left diameter of the rib cage increases, while the anteroposterior diameter decreases.

Figure 12 shows the results of the internal intercostal muscles. The displacements of the manubrium of the sternum, the middle of

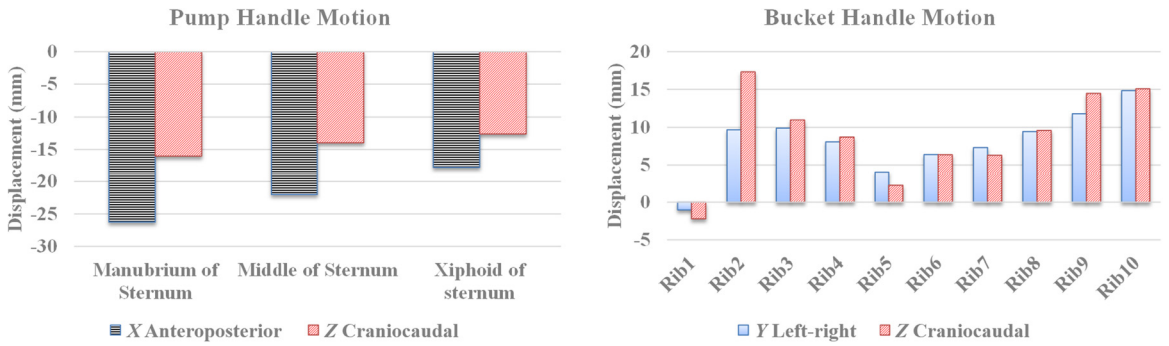

Fig. 11 Changes in pump handle motion and bucket handle motion of the ribs under the action of the dorsal external intercostal muscles

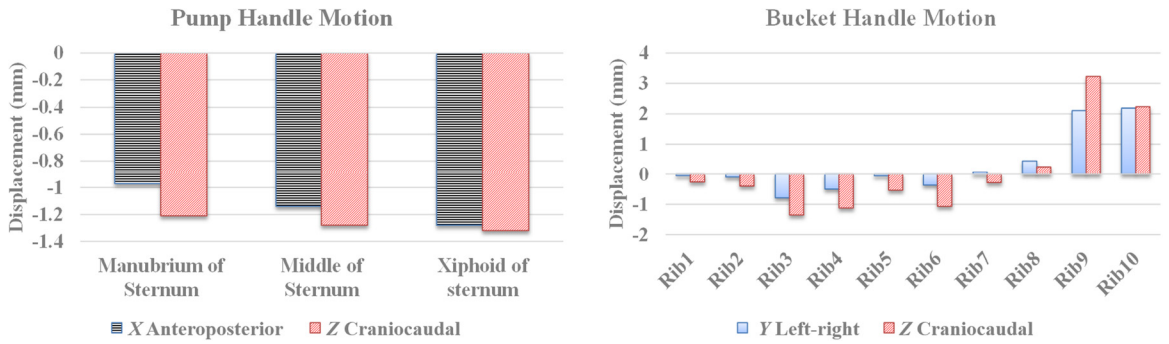

Fig. 12 Changes in pump handle motion and bucket handle motion of the ribs under the action of the internal intercostal muscles

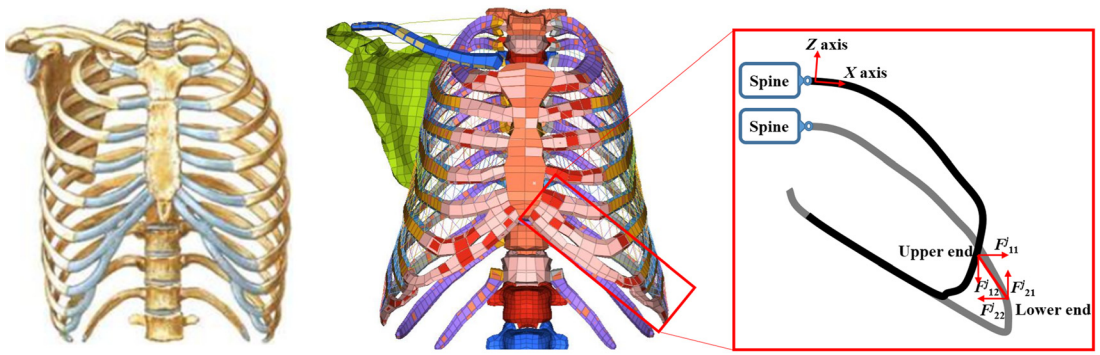

Fig. 13 Normal rib cage [47] (*a*) and the present model with rib flare (*b*)

the sternum, and the xiphoid process in the *X*-axis direction (anteroposterior direction) were –0.97, −1.14, and −1.28 mm, respectively. The displacements of ribs 1–6 in the *Y*-axis direction (lateral direction) were between −0.78 and −0.05 mm, and the displacements of ribs 7–10 were 0.08, 0.44, 2.11, and 2.19 mm, respectively. The above results illustrate that the anteroposterior and the right–left diameters of the upper ribcage decreased, while the right–left diameter of the lower ribcage increased, when the internal intercostal muscles contracted. The movement of ribs 1–6 was consistent with the findings of related studies [37,46], but the movement of ribs 7–10 was opposite to that of other ribs. The movement of ribs 7–10 might be due to the ribs flaring at the lower portion of the rib cage, which will be discussed in Sec. 3.3.4.

3.3.4 The Influence of Rib Flare. Rib flare typically affects the lower ribs and the lower edge of the rib cage (the costal arch or margin), and impairs respiratory function. Figure 13(*a*) depicts a normal rib cage and Fig. 13(*b*) represents the present model with rib flare derived from the HUMOS2 model. The influence of rib flare on chest movement during breathing was analyzed by establishing a mechanical model.

From the anteroposterior view, it can be seen that due to the rib flare, ribs 8–10 are more outward at lateral direction than the other ribs. The upper ends of the eighth and ninth intercostal muscles are close to the middle of the body and the lower ends of the eighth and ninth intercostal muscles are close to the lateral extreme of the body (Fig. 13(*b*)). When the intercostal muscles contract, a pair of forces, F^j_1 and F^j_2, are generated and can be decomposed into F^j_{11}, F^j_{12}, F^j_{21}, and F^j_{22}, F^j_{11}, and F^j_{22} are perpendicular to the outer surface of the ribs, pointing medially or laterally, respectively. F^j_{12} and F^j_{21} are perpendicular to the lower surface of the ribs, pointing to superior or inferior, respectively. Thus, F^j_{11} and F^j_{22}cause the rib to rotate around the *Z*-axis, but due to the structure of the rib cage, the joint stiffness of the *Z*-axis is much greater than that of the other two axes [42]. Therefore, the displacement on the *Z*-axis is small. F^j_{12} and F^j_{21} cause the rib to rotate around the *Y*-axis, the lateral portion of the rib elevated (Fig. 13(*b*)).

4 Conclusion

A mechanical respiratory model of chest breathing in supine position was developed based on the HUMOS2 model and Hill's active muscle model. The model took into account the influence of gravity, its validation and parameter optimization were performed by comparing with experiments. The displacement of the chest and abdomen during chest breathing was analyzed using the model. The findings demonstrated that during chest breathing, the soft tissue of the chest surface exhibited tangential displacement toward the cranial direction, and normal displacement outward during inspiration. Such motions are referred to as the bucket handle motion and the pump handle motion. However, due to the influence of the abdominal wall muscles, normal displacement in the horizontal plane of the abdominal surface increased, while normal displacement in the vertical plane of the abdominal surface decreased during inspiration.

It was also found that the dorsal portion of the external intercostal muscles contributed more to bucket handle motion than to pump handle motion, while the lateral portion of the external intercostal muscles contributed more to the pump handle motion than the bucket handle motion, and the internal intercostal muscles contributed to the expiratory motion of the rib cage. The influence of rib flare of the false ribs on rib cage movement was also discussed.

Previously, the analysis of respiratory motion of the chest and abdomen only considered the kinematics without considering power source [48,49]. This paper analyzed the coupled motion of the chest and abdomen by considering active muscle forces. The model can be used as a useful tool for estimating chest and abdomen motions in radiotherapy of visceral tumors. It can also be used in the research of respiratory motions of the patients with chronic obstructive pulmonary disease or sleep apnea syndrome. In patients with abnormal respiratory motions caused by intercostal muscle lesions, the model can help to locate the lesion. Furthermore, the model can be used to optimize the parameters of simplified respiratory motion models that are used in medical site.

Finally, it should be noted that although comparisons with experiments were conducted, further verifications are required to demonstrate the validity of the model, including the influences of mesh size, the accessory respiratory muscles as well as the motion of the lung. We will investigate the influences in future work.

Funding Data

- National Natural Science Foundation of China (Grant No.: 61871173; Funder ID: 10.13039/501100001809).
- Key R & D Plan of Hebei Province (Grant No.: 19211817D).

Nomenclature

$A(t)$ = the relationship curve between time and muscle activation level
C_{sh} = a shape parameter which determines concavity of the muscle force–length characteristics
C_{PE} = the shape parameter of the muscle force-elongation characteristics of the parallel elastic element
D_i = the distance between F^i_{12} and F^i_{21} is shown in Fig. 6
$f_a(\lambda)$ = the active force–length relationship of the muscle
F_{CE} = the forces developed by the contractile unit
F_{max} = the maximum isometric force under optimal length
F_{Mus} = the total muscle force of respiratory muscle
F_{PE} = the forces developed by the parallel unit
F_{SE} = the forces developed by the series unit
F^i_1 = the muscle force generated by the contraction of muscle fiber *i* at the rib1 end is shown in Fig. 6
F^i_{11} = the decomposed force of F^i_1 along the axis of rib1 is shown in Fig. 6
F^i_{12} = the decomposed force of F^i_1 perpendicular to the axis of rib1 is shown in Fig. 6
F^i_2 = the muscle force generated by the contraction of muscle fiber *i* at the rib2 end is shown in Fig. 6
F^i_{21} = the decomposed force of F^i_2 perpendicular to the axis of the rib2 is shown in Fig. 6
F^i_{22} = the decomposed force of F^i_2 along the axis of the rib2 is shown in Fig. 6
F^j_1 = the muscle force generated by the contraction of muscle fiber *j* at the upper rib end
F^j_{11} = the decomposed force of F^j_1 perpendicular to the outer surface of the upper rib pointing outward is shown in Fig. 13(*b*)
F^j_{12} = the decomposed force of F^j_1 perpendicular to the lower surface of the upper rib pointing downward is shown in Fig. 13(*b*)
F^j_2 = the muscle force generated by the contraction of muscle fiber *j* at the lower rib end
F^j_{21} = the decomposed force of F^j_2 perpendicular to the upper surface of the lower rib pointing upward is shown in Fig. 13(*b*)
F^j_{22} = the decomposed force of F^j_2 perpendicular to the outer surface of the lower rib pointing inward is shown in Fig. 13(*b*)
i = the number of the muscle fiber is shown in Fig. 6
M = the total moment generated by muscle fibers between rib1 and rib2
M_i = the moment generated by F^i_{12} and F^i_{21} is shown in Fig. 6
PCSA = the equivalent physiological cross-sectional area of the target muscle
α = a scaling factor to adjust the activation level of intercostal muscles
λ = the stretch ratio of the muscles
σ_{max} = the peak muscle stress value

References

[1] Roland, P. S., Rosenfeld, R. M., Brooks, L. J., Friedman, N. R., Jones, J., Kim, T. W., Kuhar, S., et al., 2011, "Clinical Practice Guideline: Polysomnography for Sleep-Disordered Breathing Prior to Tonsillectomy in Children," Otolaryngology–Head Neck Surg. Off. J. Am. Acad. Otolaryngol. Head Neck Surg., **145**(1_suppl), pp. S1–15.

[2] Jafari, P., Hoover, D. A., Yaremko, B. P., Parraga, G., and Sadeghi-Naini, A., 2019, "Incorporating Pathology-Induced Heterogeneities in a Patient-Specific Biomechanical Model of the Lung for Accurate Tumor Motion Estimation," 41st Annual International Conference of the IEEE Engineering in Medicine and Biology Society (EMBC), Berlin, Germany, July 23–27, pp. 6964–6967.

[3] Mori, S., Endo, M., Komatsu, S., Yashiro, T., Kandatsu, S., and Baba, M., 2007, "Four-Dimensional Measurement of Lung Tumor Displacement Using 256-Multi-Slice CT-Scanner," Lung Cancer, **56**(1), pp. 59–67.

[4] Spinczyk, D., Karwan, A., and Copik, M., 2014, "Methods for Abdominal Respiratory Motion Tracking," Comput. Aided Surg., **19**(1–3), pp. 34–47.

[5] Miura, H., Ozawa, S., Kawabata, H., Doi, Y., Kenjou, M., Furukawa, K., Nakao, M., and Nagata, Y., 2016, "Method of Evaluating Respiratory Induced Organ Motion by Vector Volume Histogram," Phys. Med., **32**(12), pp. 1570–1574.

[6] Semelka, R. C., Armao, D. M., Elias, J., and Huda, W., 2007, "Imaging Strategies to Reduce the Risk of Radiation in CT Studies, Including Selective Substitution With MRI," J. Magn. Reson. Imaging, **25**(5), pp. 900–909.

[7] Hostettler, A., George, D., Rémond, Y., Nicolau, S. A., Soler, L., and Marescaux, J., 2010, "Bulk Modulus and Volume Variation Measurement of the Liver and the Kidneys In Vivo Using Abdominal Kinetics During Free Breathing," Comput. Methods Prog. Biomed., **100**(2), pp. 149–157.
[8] De Troyer, A., and Wilson, T. A., 2016, "Action of the Diaphragm on the Rib Cage," J. Appl. Physiol., **121**(2), pp. 391–400.
[9] Zhang, S., Gu, L., Huang, P., and Xu, J., 2005, "Real-Time Simulation of Deformable Soft Tissue Based on Mass-Spring and Medial Representation," International Workshop on Computer Vision for Biomedical Image Applications, Berlin Germany, October, pp. 419–426.
[10] Hu, X., and Blemker, S. S., 2015, "Musculoskeletal Simulation Can Help Explain Selective Muscle Degeneration in Duchenne Muscular Dystrophy," Muscle Nerve, **52**(2), pp. 174–182.
[11] Blemker, S. S., Pinsky, P. M., and Delp, S. L., 2005, "A 3D Model of Muscle Reveals the Causes of Nonuniform Strains in the Biceps Brachii," J. Biomech., **38**(4), pp. 657–665.
[12] Inouye, J. M., Pelland, C. M., Lin, K. Y., Borowitz, K. C., and Blemker, S. S., 2015, "A Computational Model of Velopharyngeal Closure for Simulating Cleft Palate Repair," J. Craniofac. Surg., **26**(3), pp. 658–662.
[13] Lu, Y., Shen, J., Wang, C., Lu, H., and Xin, J., 2020, "Studying on the Design and Simulation of Collision Protection System Between Vehicle and Pedestrian," Int. J. Distributed Sensor Networks, **16**(1), Article No. 1550147719900109.
[14] Han, L., Dong, H., Mcclelland, J. R., Han, L., Hawkes, D. J., and Barratt, D. C., 2017, "A Hybrid Patient-Specific Biomechanical Model Based Image Registration Method for the Motion Estimation of Lungs," Med. Image Anal., **39**, pp. 87–100.
[15] Werner, R., Ehrhardt, J., Schmidt, R., and Han De Ls, H., 2009, "Patient-Specific Finite Element Modeling of Respiratory Lung Motion Using 4D CT Image Data," Med. Phys., **36**(5), pp. 1500–1511.
[16] Didier, A.-L., Villard, P.-F., Bayle, J.-Y., Beuve, M., and Shariat, B., 2007, "Breathing Thorax Simulation Based on Pleura Physiology and Rib Kinematics," International Conference on Medical Information Visualisation-BioMedical Visualisation (MediVis 2007), IEEE, Zurich, Switzerland, July 4–7, pp. 35–42.
[17] Loring, S. H., 1992, "Action of Human Respiratory Muscles Inferred From Finite Element Analysis of Rib Cage," J. Appl. Physiol., **72**(4), pp. 1461–1465.
[18] Zhang, G., Chen, X., Ohgi, J., Jiang, F., Sugiura, S., and Hisada, T., 2018, "Effect of Intercostal Muscle Contraction on Rib Motion in Humans Studied by Finite Element Analysis," J. Appl. Physiol., **125**(4), pp. 1165–1170.
[19] Behr, M., Peres, J., Llari, M., Godio, Y., Jammes, Y., and Brunet, C., 2010, "A Three-Dimensional Human Trunk Model for the Analysis of Respiratory Mechanics," ASME J. Biomech. Eng., **132**(1), p. 014501.
[20] Behr, M., Arnoux, P. J., Serre, T., Bidal, S., Kang, H. S., Thollon, L., Cavallero, C., Kayvantash, K., and Brunet, C., 2003, "A Human Model for Road Safety: From Geometrical Acquisition to Model Validation With Radioss," Comput. Methods Biomech. Biomed. Eng., **6**(4), pp. 263–273.
[21] Tropiano, P., Thollon, L., Arnoux, P. J., Huang, R. C., Kayvantash, K., Poitout, D. G., and Brunet, C., 2004, "Using a Finite Element Model to Evaluate Human Injuries Application to the HUMOS Model in Whiplash Situation," Spine, **29**(16), pp. 1709–1716.
[22] Sun, J. C., Rojas, A., Bertrand, P., Petit, Y., Kraenzler, R., and Arnoux, P. J., 2012, "Investigation of Motorcyclist Cervical Spine Trauma Using HUMOS Model," Traffic Inj. Prev., **13**(5), pp. 519–528.
[23] Rotaru, G.-M., Pille, D., Lehmeier, F., Stämpfli, R., Scheel-Sailer, A., Rossi, R., and Derler, S., 2013, "Friction Between Human Skin and Medical Textiles for Decubitus Prevention," Tribol. Int., **65**, pp. 91–96.
[24] Roussos, C., Fixley, M., Genest, J., Cosio, M., Kelly, S., Martin, R., and Engel, L., 1977, "Voluntary Factors Influencing the Distribution of Inspired Gas," Am. Rev. Respir. Disease, **116**(3), pp. 457–467.
[25] Dail, C. W., 1956, "Muscle Breathing Patterns," Med. Arts Sci., **2**, pp. 64–70.
[26] Ratnovsky, A., and Elad, D., 2005, "Anatomical Model of the Human Trunk for Analysis of Respiratory Muscles Mechanics," Respir. Physiol. Neurobi., **148**(3), pp. 245–262.
[27] Hill, A. V., 1938, "The Heat of Shortening and the Dynamic Constants of Muscle," Proc. R. Soc. London. Ser. B-Biol. Sci., **126**(843), pp. 136–195.
[28] De Troyer, A., and Estenne, M., 1988, "Functional Anatomy of the Respiratory Muscles," Clin. Chest Med., **9**(2), pp. 175–193.
[29] Han, J., Gayan-Ramirez, G., Dekhuijzen, R., and Decramer, M., 1993, "Respiratory Function of the Rib Cage Muscles," Eur. Respir. J., **6**(5), pp. 722–728.
[30] Drake, R., Vogl, A. W., and Mitchell, A. W., 2009, *Gray's Anatomy for Students*, Elsevier Health Sciences, North York, ON, Canada.
[31] Romero, F., and Alonso, F. J., 2016, "A Comparison Among Different Hill-Type Contraction Dynamics Formulations for Muscle Force Estimation," Mech. Sci., **7**(1), pp. 19–29.
[32] Ju, S., Lee, S. J., Park, M. J., Cho, Y. J., Jeong, Y. Y., Jeon, K. N., Bae, K., Lee, J. D., and Kim, H. C., 2018, "Clinical Importance of Cross-Sectional Area of Intercostal Muscles in Patients With Chronic Obstructive Pulmonary Disease," Clin. Respir. J., **12**(3), pp. 939–947.
[33] Close, R. I., 1972, "Dynamic Properties of Mammalian Skeletal Muscles," Physiol. Rev., **52**(1), pp. 129–197.
[34] Yoshida, R., Tomita, K., Kawamura, K., Nozaki, T., Setaka, Y., Monma, M., and Ohse, H., 2019, "Measurement of Intercostal Muscle Thickness With Ultrasound Imaging During Maximal Breathing," J. Phys. Ther. Sci., **31**(4), pp. 340–343.
[35] Winters, J. M., and Stark, L., 1988, "Estimated Mechanical Properties of Synergistic Muscles Involved in Movements of a Variety of Human Joints," J. Biomech., **21**(12), pp. 1027–1041.
[36] Ratnovsky, A., Zaretsky, U., Shiner, R. J., and Elad, D., 2003, "Integrated Approach for In Vivo Evaluation of Respiratory Muscles Mechanics," J. Biomech., **36**(12), pp. 1771–1784.
[37] Wilson, T. A., Legrand, A., Gevenois, P.-A., and Troyer, A., 2001, "Respiratory Effects of the External and Internal Intercostal Muscles in Humans," J. Physiol., **530**(2), pp. 319–330.
[38] Winters, J. M., and Stark, L., 1985, "Analysis of Fundamental Human Movement Patterns Through the Use of in-Depth Antagonistic Muscle Models," IEEE Trans. Biomed. Eng., **BME-32**(10), pp. 826–839.
[39] Inouye, J. M., and Blemker, S. S., 2015, "Advances in Hyperelastic Finite Element Modeling of Biological Tissues: Explicit Strain Energy Function Specification," 39th Annual Meeting of the American Society of Biomechanics, Columbus, OH, Aug. 5–8, pp. 1–2.
[40] Wittek, A., and Kajzer, J., 1997, "Modelling of Muscle Influence on the Kinematics of the Head-Neck Complex in Impacts," Memoirs-School Eng. Nagoya Univ., **49**, pp. 155–205.
[41] Zeng, W., Mukherjee, S., Caudillo, A., Forman, J., and Panzer, M. B., 2021, "Evaluation and Validation of Thorax Model Responses: A Hierarchical Approach to Achieve High Biofidelity for Thoracic Musculoskeletal System," Front. Bioeng. Biotechnol., **9**, p. 633.
[42] Duprey, S., Subit, D., Guillemot, H., and Kent, R. W., 2010, "Biomechanical Properties of the Costovertebral Joint," Med. Eng. Phys., **32**(2), pp. 222–227.
[43] Ward, M. E., Ward, J. W., and Macklem, P. T., 1992, "Analysis of Human Chest Wall Motion Using a Two-Compartment Rib Cage Model," J. Appl. Physiol., **72**(4), pp. 1338–1347.
[44] Zhang, G. Z., Chen, X., Ohgi, J., Miura, T., Nakamoto, A., Matsumura, C., Sugiura, S., and Hisada, T., 2016, "Biomechanical Simulation of Thorax Deformation Using Finite Element Approach," Biomed. Eng. Online, **15**(1), pp. 1–18.
[45] Sampson, M. G., and Troyer, A. D., 1982, "Role of Intercostal Muscles in the Rib Cage Distortions Produced by Inspiratory Loads," J. Appl. Physiol. Respir. Environ. Exer. Physiol., **52**(3), pp. 517–523.
[46] Ratnovsky, A., Elad, D., and Halpern, P., 2008, "Mechanics of Respiratory Muscles," Respir. Physiol. Neurobiol., **163**(1–3), pp. 82–89.
[47] Netter, F. H., 2014, Atlas of Human Anatomy, Elsevier Health Sciences, Philadelphia America.
[48] McClelland, J. R., Hawkes, D. J., Schaeffter, T., and King, A. P., 2013, "Respiratory Motion Models: A Review," Med. Image Anal., **17**(1), pp. 19–42.
[49] Lei, L., Huang, L., Zhao, B. L., Hu, Y., Jiang, Z. L., Zhang, J. W., and Li, B., 2021, "Diffeomorphic Respiratory Motion Estimation of Thoracoabdominal Organs for Image-Guided Interventions," Med. Phys., **48**(8), pp. 4160–4176.